



HAL
open science

Effect of microstructure on hydric strain in clay rock: A quantitative comparison

Anne-Laure Fauchille, Stephen Hedan, Valery Valle, Dimitri Pret, Justo Cabrera, Philippe Cosenza

► To cite this version:

Anne-Laure Fauchille, Stephen Hedan, Valery Valle, Dimitri Pret, Justo Cabrera, et al.. Effect of microstructure on hydric strain in clay rock: A quantitative comparison. Applied Clay Science, 2019, 182, pp.105244. 10.1016/j.clay.2019.105244 . hal-02301531

HAL Id: hal-02301531

<https://hal.science/hal-02301531>

Submitted on 20 Jul 2022

HAL is a multi-disciplinary open access archive for the deposit and dissemination of scientific research documents, whether they are published or not. The documents may come from teaching and research institutions in France or abroad, or from public or private research centers.

L'archive ouverte pluridisciplinaire **HAL**, est destinée au dépôt et à la diffusion de documents scientifiques de niveau recherche, publiés ou non, émanant des établissements d'enseignement et de recherche français ou étrangers, des laboratoires publics ou privés.



Distributed under a Creative Commons Attribution - NonCommercial 4.0 International License

27 **Abstract**

28 This paper presents a new method able to compare quantitatively strains and microstructure
29 of a clay material. This method was applied to a Tournemire clay rock sample subjected to
30 cyclic hydric loading in laboratory conditions. Local strains of a centimeter-size
31 Tournemire clay rock sample were quantified by digital image correlation (DIC) on a field
32 of view of 5.5 x 4.1 mm² at the resolution of 2 $\mu\text{m}\cdot\text{pixel}^{-1}$, at a temperature of 22°C and
33 between 98 and 33% of relative humidity. At the end of the hydric loading, at dry state, the
34 microstructure of the same field of view was mapped by an extended mosaic of scanning
35 electron microscopy images at the resolution of 0.625 $\mu\text{m}\cdot\text{pixel}^{-1}$ and superimposed to the
36 reference images used for DIC. Two microstructural parameters: the mean area and the area
37 fraction of rigid clasts and clay matrix, were quantified by image analysis to be directly
38 superimposed to local strain values. Speckle artefacts partly due to polished surfaces of
39 clasts were filtered in the comparison between strains and microstructure. Strains
40 concentrated in parts of the clay matrix, and at the interface between matrix and several
41 quartz clasts which showed a slight detachment from the matrix. Constant clay and clast
42 area fractions and sizes corresponded to very variable strain values at the microstructure
43 scale. The relationship between strain values, mineral size and area fractions was not linear.
44 Micro-mechanisms of deformation were therefore very complex at the scale of the
45 experiment. On a very large field of view, very different microstructure behaviors were
46 averaged which avoided any simple relationship between microstructure and strains.
47 Heterogeneous water distribution and non-local microstructural control factors were
48 suspected.

49 **Keywords:**

50 Hydric loading, strain, Tournemire clay rock, microstructure, phase area fraction, Digital
51 Image Correlation

52

53 **1. Introduction**

54 Clay rocks are interesting underground media for high-level radioactive waste repositories
55 in several industrial countries around the world. The storage capabilities are mainly due to a
56 very low intrinsic permeability and thermo-hydro-mechanical and chemical properties of
57 clays which form radiation-proof and fluid-proof barriers for wastes over the next centuries.
58 The optimization of the long term safety of this type of repository is strongly related to the
59 understanding of deformation mechanisms of the host material at the basin scale, but also in
60 the excavation damaged zone (EDZ) around galleries at the repository scale (Cabrera et al.,
61 2001; Matray et al., 2007; Möri et al., 2010). The initiation and extension of EDZ are
62 governed by a high variability of parameters such as the mineralogy, the anisotropy, the
63 initial stress field, the existence of preexisting fractures and weak joints, the repository's
64 geometry and the hydric state of galleries (Bossard et al., 2002, 2017; Tsang et al., 2005;
65 Blüming et al., 2007; Hédan et al., 2014, 2018). During both digging and operational
66 phases, clay rocks are subjected to various stimulations such as mechanical damages,
67 temperature and humidity variations, fluid flow, swelling and shrinkage, which can be
68 monotonic or cyclic over months to years. Understanding of the deformation mechanisms
69 of EDZ is therefore a critical issue to minimize the risk assessment of underground nuclear
70 waste storage in argillaceous formations.

71 Clay rocks are heterogeneous and multiscale materials. The macroscopic deformation is
72 generally controlled by microscopic effects at smaller scales, mainly due to their
73 sedimentary pattern and geological history. The quantitative response of clay rocks to
74 loadings representative of EDZ events is currently poorly understood, especially for hydric
75 loadings. Despite of challenging works performed by Wang et al. (2013, 2014) in which
76 heterogeneous strain fields of Callovo-Oxfordian clay rocks from the Paris basin were
77 acquired by digital image correlation and compared with the microstructure under

78 environmental electronic microscopy, the current literature conclusions regarding the link
79 between strains and microstructure are mostly qualitative and focus on very limited areas.
80 This study provides a first experimental investigation of the quantitative effects of a hydric
81 loading on strains and microstructure of clay rock, on a millimeter size field of view in high
82 resolution. A case study is presented on a Tournemire clay rock sample, from the
83 Underground Research Laboratory (URL) of Tournemire in Aveyron, France.
84 Clay rocks are composed of clasts, mainly quartz, carbonates, feldspars and sulfur oxides,
85 surrounded by a matrix composed of clay minerals more or less orientated. At the
86 microscale, strains of Callovo-Oxfordian clay rocks subjected to hydric processes have
87 been qualitatively linked to high area fractions of clay matrix and limited area fractions of
88 rigid silica and carbonates, (Montes et al., 2004; Yang et al., 2012; Wang, 2012). This
89 paper provides a quantitative comparison between strains and local area fractions and sizes
90 of clasts and clay matrix at the microstructure scale, during a hydric loading representative
91 of accelerated humidity conditions of the URL galleries. The objectives of this paper are to
92 present (a) a method which allows the quantitative comparison between microstructure and
93 strains, and (b) an application on Tournemire clay rock.

94 **2. Material and Methods**

95 **2.1. Tournemire clay rock**

96 The sample used in this study comes from the Upper Toarcian formation from the
97 Tournemire (URL) of the Institute for Radioprotection and Nuclear Safety (IRSN) in
98 Aveyron, France. The sample comes from the borehole FD90 (depth of 4.20-4.40 m) in the
99 1997 East Gallery (Fauchille et al., 2016a). The Tournemire URL was excavated in a
100 sedimentary basin composed of sub-horizontal consolidated argillaceous Toarcian and
101 marly Domerian layers, located on the southern border of the French Massif Central
102 (Bonin, 1998; Cabrera et al., 2001; Constantin et al., 2002). The mineralogical composition

103 of the argillaceous rocks from the upper Toarcian layers is mainly 40 wt% clay minerals,
104 illite (5-15 wt%), illite/smectite mixed-layer minerals (5-10 wt%), chlorite (1-5 wt%) and
105 kaolinite (15-20 wt%), 10-20 wt% of quartz grains, 10-40 wt% of carbonates (mainly
106 calcite), and 2-7 wt% of pyrite (Bonin, 1998; De Windt et al., 1998; Cabrera et al., 2001).

107 **2.2. Methods**

108 **2.2.1. Hydric loading**

109 A cubic clay rock sample of 20x20x20 mm³ was subjected to a desaturation-saturation-
110 desaturation cycle in a waterproof box at controlled relative humidity (RH) and temperature
111 (T). The sample was initially carefully polished with carbide and diamond products, and
112 saturated at RH=98% with a saline solution of CuSO₄, 5H₂O and at T=22°C (temperature
113 sensor Testo 175 H1 allowing recording RH at ±2% and T at ±0.3°C) for two months. It was
114 then desaturated at RH=33% at the same temperature with a saline solution of MgCl₂, then
115 resaturated at 98% and desaturated again at RH=33% (Figure 1a). After the cyclic loading,
116 the sample was subjected to a last desaturation at very low RH (3-5%) with a container of
117 P₂O₅ placed inside the box. During the hydric process, the sample was placed on a precision
118 balance Adam PGW 753E (precision ±0.002 g). The weight of the sample at RH=3-5% was
119 taken as reference for the dry state of the sample, to calculate the mean water content along
120 the process. The water content of the sample is therefore underestimated in comparison
121 with water content values around 5% found in the literature and determined after oven-
122 drying for 48 hours at 105°C (Cabrera et al., 2001). Two sample's faces were filmed by
123 optical cameras of 5 Mp (2560x1980 pixels) equipped by a telecentric lens (Figure 2). A
124 first view was composed of an entire sample's face and was filmed at a resolution of 10
125 μm.pixel⁻¹. A second view of 5.5 x 4.1 mm² from a part of another face was captured in
126 time at the resolution of 2.2 μm.pixel⁻¹. Beddings planes are in the vertical direction for the
127 first view, and in the horizontal direction for the second view (Figure 2). This paper focuses

128 on the methodology and results linked to the second view only (Figure 2). A spot light of
129 400 W was placed next to the waterproof box. It was switched on 2 sec before the image
130 capture and switched off afterwards. Images were taken every 30 seconds to 30 minutes
131 during 55 days, depending on the experiment steps. Images were analyzed by Digital Image
132 Correlation (DIC) in order to calculate hydric strains.

133 The time steps of the loading were defined as a function of stabilized mean water content
134 and strains (Figure 1b,c). The drop of relative humidity after the saturation phase is due to
135 an accidental slight opening of the box containing the setup. As a consequence only
136 desaturation phases are analyzed in the manuscript. Oscillating mean water contents were
137 due to little cycles of temperature during night and working time though (Figure 1b).

138 After the completed hydric process, the microstructure of the sample was characterized by a
139 mosaic of back scattered electron images under SEM in order to superimpose
140 microstructure and strains calculated by DIC (Figure 2). The main advantage of the
141 desaturation at RH= 5% explained above is to desiccate smoothly the sample before being
142 analyzed under SEM. Observation under SEM requires the sample desaturation to acquire
143 high quality imaging and avoid any damage of both the machine and the sample. Additional
144 details of the experimental setup are available in Fauchille et al., (2016a).

145 **2.2.2. Digital image correlation (DIC)**

146 DIC is an optical full field measurement method, used on a vast range of materials (metallic
147 alloys, glasses, fluids, geomaterials...) and for many industrial and research applications
148 including geomechanics (Sutton et al., 1983; Bruck et al., 1989; Desrues et al., 1985; Valès,
149 2008, Bornert et al., 2010). It is a non-invasive and a non-destructive method which allows
150 the evaluation of the displacement full-field of a 2D surface. It is performed from the
151 quantitative comparison of image partitions called subsets, from a reference image to a
152 deformed image. The comparison of subsets is based on the comparison of grey levels (8

153 bit) between an initial image and a final one, modified by a specific kinematical
 154 transformation. The optical images of the sample during the hydric process were analyzed
 155 by an improved DIC method called H^kDIC and developed by Valle et al., (2015). The
 156 software used was X-Correl. This method allows the displacement calculation in the
 157 presence of single and or crossed cracks in subsets. It can give accurately the displacements
 158 near a crack, without knowing the crack distribution or position. In this study,
 159 displacements were calculated in subsets from 32 to 64 pixels, which correspond to 70.4 to
 160 140.8 μm, respectively. Strains were calculated by displacement derivation for steps of 2
 161 pixels (Hédan et al., 2014; Fauchille et al., 2016a). In this study, results are presented for
 162 main strains ε_1 and ε_2 (Equations 1,2).

$$\varepsilon_1(x, y) = \frac{\varepsilon_{xx}(x, y) + \varepsilon_{yy}(x, y)}{2} + \frac{\varepsilon_{xy}(x, y)}{\sin(2\theta)} \quad (1)$$

$$\varepsilon_2(x, y) = \frac{\varepsilon_{xx}(x, y) + \varepsilon_{yy}(x, y)}{2} - \frac{\varepsilon_{xy}(x, y)}{\sin(2\theta)} \quad (2)$$

$$\text{with } \theta = \frac{1}{2} \arctg \frac{2\varepsilon_{xy}(x, y)}{\varepsilon_{xx}(x, y) - \varepsilon_{yy}(x, y)}$$

163 $\varepsilon_{xx}(x, y)$, $\varepsilon_{yy}(x, y)$ and $\varepsilon_{xy}(x, y)$ are calculated by displacement derivation on neighbour
 164 subsets. Strain fields were determined with an increment of 1 pixel between two subsets.
 165 The sample's speckle is natural and no additional painting was used. An image of the
 166 speckle is available in the Supplementary Material part of this paper (Appendix 1). Surface
 167 roughness and visible polished clasts within the clay matrix are the only markers on the
 168 sample's surface. The standard deviation σ_{sk} of grey levels was calculated in all subsets of
 169 the analyzed images (Equation 3), in order to control the speckle evolution during the
 170 hydric loading.

$$\sigma_{sk}(x, y) = \sqrt{\frac{1}{(D+1)^2} \sum_{i=x-\frac{D-1}{2}}^{x+\frac{D-1}{2}} \sum_{j=y-\frac{D-1}{2}}^{y+\frac{D-1}{2}} (f(i, j) - \overline{f(x, y)})^2} \quad (3)$$

171 D is the size of the subset (here 32 to 64 pixels), $f(i, j)$ is the grey level function for the
 172 coordinates (i, j) , and $\overline{f(x, y)}$ is the mean grey level on the subset for the coordinates
 173 (x, y) .

174 Due to the fact that the microstructure of the sample was characterized at a dry state and the
 175 presence of cracks at the beginning of the test (Fauchille et al., 2016a), the reference images
 176 for DIC were chosen at the end of desiccation steps at t_{0-1} and t_{0-2} (Figure 1a). At t_{0-1} and t_{0-2} ,
 177 hydric cracks are closed and the sample is partially desaturated. These steps are therefore
 178 used as hydric-stable reference steps. The deformed images were chosen at the beginning of
 179 the test at t_1 with open cracks and partial saturation and at the beginning of the second
 180 desaturation at t_2 . This configuration allows an optimized comparison between the highest
 181 desiccation strains (Figure 1b) and microstructure.

182 Out-of-plane tests of digital image correlation were performed in the validation phase of the
 183 experimental setup. The results revealed that a displacement of the sample of -0.2 mm to
 184 +0.2 mm towards to away from the camera did not disturb the measurements of local
 185 displacements (Fauchille, 2015). In other words, a shrinkage or swelling of the sample of
 186 $\pm 1\%$ in the out-of-plane direction of the surface observed is not noticeable with the optical
 187 configuration chosen. The subsets of 32×32 pixels to 64×64 pixels always contain clay-
 188 matrix and clasts. In this configuration, the DIC code cannot distinguish any difference
 189 between small displacement of individual clasts and local strains.

190 **2.2.3. Characterization of Microstructure by a mosaic of images under a scanning** 191 **electron microscope (SEM)**

192 At the end of the second desiccation, the sample was placed into a desiccator at RH=5%.

193 Then at t_{SEM} (Figure 1b) a surface of 7.1 mm x 5.5 mm including the surface of 5.5 x 4.1
194 mm² previously filmed by the camera was scanned under SEM, by a mosaic of 153 back-
195 scattered electron (BSE) images of 1024x768 pixels at a resolution of 0.625 $\mu\text{m}/\text{pixel}$. Note
196 here that the sample's deformation between t_{0-2} and t_{SEM} was considered negligible due to
197 the shrinkage curve of clay materials. In other words, the sample's water content between
198 t_{0-2} and t_{SEM} was below the so-called shrinkage limit of Tournemire clay rock (Boisson et
199 al., 2001). Images were overlapping in area of 11% in the horizontal direction and 14% in
200 the vertical direction to have an excellent correspondence from an image to the following in
201 both directions. The electron beam drift was taken into account to assemble correctly all
202 images (Fauchille, 2015). The image acquisition was performed on SEM JEOL 5600 LV
203 equipped by Bruker Esprit software. The acquisition parameters were a voltage of 15 kV,
204 a magnification x200, and a working distance of 16.3 mm. BSE images are composed of 256
205 different grey levels (8bits), in which each grey level represents a mean atomic number and
206 a local mean mineralogical composition. The image acquisition was performed with an
207 optimized BSE contrast with a well-defined histogram of grey levels to facilitate the further
208 phase segmentation. At the resolution of 0.625 $\mu\text{m}\cdot\text{pixel}^{-1}$, this mode allows a well
209 distinction of clay matrix and micrometer-scale clasts (Appendix 2). The clay matrix is
210 defined at the mesoscopic scale as the homogeneous ground mass of the clay rock, mainly
211 composed of fine clay minerals and clasts smaller than 0.625 μm .

212 **2.2.4. Quantitative characterization of microstructure**

213 *Phase segmentation*

214 The mineralogical phases were segmented on the reconstructed mosaic of BSE images by
215 the in-house software MicroPhaseMap (Prêt et al., 2010a,b), according to the histogram of
216 8 bit grey levels and the variance filter. The clay matrix, clasts composed of quartz,
217 carbonates and heavy minerals, and macropores were considered (Appendix 3). Note here

218 that the clay matrix included small clasts smaller than 0.625 μm because it depends on the
 219 scale and the resolution of the study.

220 ***Quantitative parameters***

221 From the segmented mosaic of BSE images, quantitative parameters were calculated to
 222 describe the microstructure. The area, length ratio and orientation of each type of clast were
 223 calculated by ImageJ software and in-house codes (Fauchille et al., 2018). The area of a
 224 clast corresponds to the total number of its pixels. In the same subsets than those previously
 225 used for DIC, the area fraction P_D (Equation 4) is calculated:

$$P_D(x, y) = \frac{1}{(D + 1)^2} \sum_{n=x-\frac{D-1}{2}}^{n=x+\frac{D-1}{2}} \sum_{m=y-\frac{D-1}{2}}^{m=y+\frac{D-1}{2}} G_{(n,m)} \quad (4)$$

226 $G_{(n,m)}$ is the indicator function and equal to 0 or 1 (1 when the pixel (n, m) corresponds to
 227 the segmented phase and 0 else). D is the size of the subset.

228 The area fraction of a chosen phase p in a square subset of $D \times D$ pixels is the ratio of
 229 pixels which correspond to the chosen phase by the total number of pixels in the subset. It
 230 is thus included between 0 and 1 (or 0 and 100%). P_D was calculated with the pixels of
 231 mineral phases included in the subsets (grey part in Figure 3a).

232 Each clast is characterized by a fixed area. The mean area of clasts \bar{A}_D (Equation 5) which
 233 characterizes every subset (x,y) was calculated by taking into account all clasts totally and
 234 partially included in the subset (grey part in Figure 3b).

235

$$\bar{A}_D(x, y) = \frac{1}{N_{(x;y)}} \sum_{i=1}^{i=N_{(x;y)}} A_i \quad \text{if } N_{(x;y)} \geq 1 \quad (5)$$

$$\bar{A}_D(x, y) = 0 \quad \text{if } N_{(x;y)} = 0$$

236 $N_{(x;y)}$ is the number of clasts in the subset centered in (x;y). A_i is the area of the clast i
237 (carbonate, quartz or heavy minerals) in the subset centered in (x;y).
238 The mean area of clasts is the ratio of the sum of areas of the clasts present in the subset by
239 the total number of clasts in the same subset.
240 The comparison between strains and microstructure was also tested with other
241 microstructure configurations (for example by choosing the clasts only with a center
242 included in the subset), but the two configurations in Figure 3 were considered more
243 representative of the local microstructure. The comparison of strain values with \bar{A}_D and P_D
244 requires an excellent superimposition between the optical image at $t_{0.2}$ used for DIC (Figure
245 1b), and the mosaic of SEM images. To quantify the error of superimposition between these
246 images, the distances between the center of 4 markers (well-visible clasts and macropores)
247 were measured on both images with Deftac software. The mean error of clast position is in
248 the order of 2.3 μm , that is to say that a clast localized on the reference optical image can
249 be in theory at a distance of $\pm 2.3 \mu\text{m}$ around on the SEM images.

250 ***2D Mapping***

251 The 2D mapping of area fractions and mean area involves the calculation of the values of
252 area fractions and clast's area on each subset's coordinates. This method brings an extended
253 view of local heterogeneities and multiscale interfaces of the microstructural parameters
254 calculated (Fauchille et al., 2014, 2018). The maps of area fractions and mineral's mean
255 area have the same dimensions than the strain fields calculated by DIC. The hydric strain
256 values are therefore superimposed one by one to a value of mineral area fraction and clast
257 mean area. Note here that the comparison between microstructure and strains in the subsets
258 can be performed in larger subsets and therefore may depend on the subset size. However
259 for much larger subsets, strains, area fractions and mean areas tend towards mean values of
260 the entire map. For small subsets, the distribution of phase area fraction tends towards a

261 bimodal distribution due to the segmentation of 100% of clay matrix or 100% of clasts. The
262 comparison between strains and microstructure is therefore presented for the same subset
263 size.

264 **3. Results**

265 **3.1. Heterogeneous strain fields at the microstructure scale**

266 Hydric strains were highly variable in space during the hydric process. An example of the
267 main strain fields at t_1 compared to t_{0-1} is represented in Figure 4, for a subset of 32 pixels.
268 Three main hydric cracks (indicated by black arrows in Figure 4a) separated by around one
269 millimeter distance were detected, especially on ϵ_1 field (Figure 4 a,b).

270 Discontinuous concentrations of high strains > 0.05 or < -0.05 of ϵ_1 and ϵ_2 , respectively,
271 were locally detected by blue to purple and yellow to red colors (Figure 4 c,d). These high
272 strains were separated by more homogeneous zones in which strains are close to zero,
273 represented in green color. Strain values were very heterogeneous, but the spatial
274 distribution of strain values was also heterogeneous among the sample's surface. Aside
275 from the three main cracks, several areas were high strain-richer than others in which the
276 deformation was more diffused. For example, the red zones 1 and 2 in Figure 4a contained
277 heterogeneous strains including high, low and homogeneous strains, respectively. The
278 results were similar for the desaturation between t_2 and t_{0-2} but the three main cracks
279 showed a much limited aperture.

280

281 **3.2. Variability of microstructure at the mm scale**

282 The distribution of the clast area fraction (P_{clasts}) was calculated for three sizes of subsets:
283 32x32, 48x48 and 64x64 pixels (Figure 5a). The area fractions were calculated with a step
284 of 1 pixel, which caused the smoothing of the distributions but did not change the
285 maximum of the curves. For the three subset's sizes, the distribution of area fractions

286 showed a range of variable values included in [0.02 ; 0.9], which corresponded to 2% to
287 90% of clasts. There was therefore no subset which contained 100% of clays or 100% of
288 clasts. For subset sizes between 32 to 64 pixels, the clast fraction distributions are the
289 highest at 0.18 to 0.22 (red peaks in Figure 5a), so subsets which contain around 20% of
290 clasts and 80% of clay matrix were the most common on the sample's surface. The three
291 peaks were closer to 0 than 1, so the sample's surface contained more clay-rich than clast-
292 rich subsets, for any subset size. The location of P_{clast} values shown in Figure 5a was
293 represented in a 2D map for a subset of 32 pixels in Figure 5b. As strains have been
294 previously presented, the microstructural parameters of P_{clast} and A_{clast} were very
295 heterogeneously distributed among the sample's surface. Several areas showed very low
296 concentrations of clasts ($P < 0.2$) whereas localized areas were characterized by area
297 fractions higher than 0.5. The area fractions higher than 0.5 corresponded qualitatively to
298 zones which are rich in large clasts (Figure 5c). It was particularly visible for clasts larger
299 than 1500 pixels, which is equivalent to a mean diameter of 44 pixels in case of circular
300 grains. High concentrations of large clasts were often surrounded by abrupt concentrations
301 of small clasts, probably due to the fact that large grains were taken into account in
302 different subsets in \bar{A}_{32} calculation (Figure 3b). Large clast-rich zones were consequently
303 more localized and discontinuous on the map, contrary to the area fractions previously
304 mapped.

305 **3.3. Relationship between microstructure and speckle**

306 The strain field of ε_2 was superimposed to the microstructure in Figure 6. Results were
307 similar for ε_1 . The superimposition of ε_2 to the microstructure showed that the strain
308 concentrations were both present in the clay matrix, at the interface between clasts and clay
309 matrix, and crossed individual or aggregates of large quartz and carbonates (Figure 6 b,c).
310 Qualitatively, strains smaller than 0.05 represented in green color were located on the clay

311 matrix with limited size clasts (Figure 6c). Nevertheless, large and round clasts of
312 carbonates and quartz located in Figure 6b were partly characterized by surprising strains
313 higher than 0.05 (blue to purple color in Figure 6c) for the humidity and temperature
314 conditions of the experiment. On the whole strain fields at t_1 and t_2 , high strains values of ε_1
315 and ε_2 did not correspond to clay matrix-rich areas only and low strains to quartz and
316 carbonate-rich areas. The relationship between strain and microstructure seemed to be more
317 complex than expected. The speckle evolution was then investigated to explain the presence
318 of abnormal high strains on rigid particles, usually inert to water during this type of hydric
319 loading (Figure 7). Figure 7a is an extract of the optical images during the hydric loading,
320 showing how the speckle on the sample's surface changes in time. The surface showed
321 particular changes of local contrast, on areas smaller than the subset's size. Homogeneous
322 brightness drifts were taken into account in the DIC code in the minimization of the
323 correlation coefficient, but not the local contrast. The 2D maps of the standard deviation of
324 grey levels σ_{sk} in subsets of 32 pixels were calculated at t_1 and t_2 . The map of σ_{sk} at t_2
325 (which represents the grey level variations between t_{0-2} and t_2) is shown in Figure 7b
326 (Equation 3). This map demonstrates that the speckle changes was located in diffuse areas
327 for σ_{sk} between 0 and 0.02 and in specific areas for σ_{sk} higher than 0.02, heterogeneously
328 distributed on the surface. The location of those areas was sometimes correlated to zones
329 already characterized by a high area fraction or by a high mean area of carbonates and
330 quartz (Figure 5 b,c). However, plenty of zones presenting a standard deviation of grey
331 levels higher than 0.02 did not show any correlated strain value. The speckle changes' map
332 was then superimposed to the microstructure (Figure 7c to e). High variations of speckle
333 were qualitatively correlated to the presence of relatively large and round clasts but very
334 elongated carbonates did not show any particular strain concentrations (Figures 7e, 6c).
335 Figures 6c and 7f have highlighted that high strains and important speckle changes

336 corresponded to large clasts (carbonate, quartz, pyrite) which did not show any deformation
337 evidence on the SEM images. Lower but significant values of σ_{sk} were both characterized
338 by quartz grains surrounded by a local roughness, porous clay matrix aggregates due to
339 sample's shrinkage (red circles). Destroyed clay matrix in microaggregates and microcracks
340 were also detected. However the porous matrix aggregates did not always correspond to
341 significant strain or speckle changes, which leaves the possibility that those aggregates
342 formed during and or after the hydric loading. σ_{sk} was then directly compared to the mean
343 area of clasts (Figure 8a). Figure 8a has revealed that a constant area of clasts was related to
344 very different speckle changes. However the standard deviation of grey levels slightly
345 increased from 0.01 to 0.015 with increasing clast sizes. According to the optical images
346 (Figure 7a), polished areas of large clasts might correspond to smoother and blurrier
347 surfaces on the optical images, with a lower local contrast. Consequently the local changes
348 of speckle and strains were partly explained by two effects:

349 (i) several large clasts had a well plane surface due to the initial polishing which avoided
350 DIC to determine accurately local displacements and strains, which increased the error of
351 strain values

352 (ii) the clasts of quartz were subjected to a slight rotation and detachment caused by the
353 clay matrix shrinkage on their boundaries. It was not observed on carbonate because their
354 texture was more cemented and tortuous contrary to quartz which were individual and
355 rounder grains (Fauchille, 2015). The effect of (i) on speckle and strain was significantly
356 higher than (ii).

357 Figure 8b represents the distribution of σ_{sk} values for the two desaturation steps. For the
358 second desaturation, the number of subsets characterized by a $\sigma_{sk} > 0.0185$ (which
359 corresponds to the crossing point of the two plots in Figure 8b) was 1.44 times higher than
360 for the first one. The speckles changes were quantitatively more important during the

361 second desaturation. The subsets with a $\sigma_{sk} > 0.02$ were then filtered and not considered in
362 the comparison of strains and microstructure. 0.02 corresponded to the slope change after
363 the peak of normalized frequency. These remaining pixels represented 86.6% of the total
364 number of pixels.

365 Another possibility to interpret high strains in clast-supported regions was that larger voids
366 filled by water at the end of saturation in those regions were drained before the isolated
367 matrix pores, due to their size. In this case there was a time interval between the desiccation
368 of the matrix around those pores and other locations, due to local porosity heterogeneities.
369 Those pores might have lead to larger strains between rigid clasts and matrix during
370 moistening and eventually resulted in some strain reversal during desiccation. This
371 interpretation is supported by Philip et al., (2017) who have seen that clast-rich regions
372 could hold open larger pores in Opalinus Clay, potentially being filled with water earlier
373 than the surrounding matrix pores.

374 **3.4. Quantitative comparison between strains and microstructure**

375 The quantitative comparison of filtered strain values and microstructural parameters was
376 shown for the first desaturation between t_{0-1} and t_1 in Figure 9 a,b. Results were similar for
377 the second desaturation but the first one was considered the most representative due to a
378 better speckle conservation. For subsets of 32 pixels, the areas fractions P_{clast} bellow 0.25
379 corresponded to a high variability of strain values, from -0.025 to 0.075. Strain variability
380 decreased with increasing P_{clasts} . The relationship between strain and P was not linear.
381 Comparisons with different subsets sizes for strains and microstructure were tested but the
382 results were similar and no linear tendency was highlighted. An example was given for
383 subsets of 64 pixels (Figure 9b). The subset size did not control the link between
384 microstructure and strain, at the scale of the study. Quartz and carbonate area fractions were
385 separately compared to strains (Figure 9c). Area fractions above 0.1 were associated to

386 decreasing strains and low area fractions, which represented higher area fractions of clay
387 matrix. Quartz and carbonate area fractions below 0.1 were associated to very variable
388 strain values. Neither local quartz or carbonate concentration only controlled the
389 deformation of the sample. Large clasts corresponded to low strain (Figure 9d) but subsets
390 composed of lots of small clasts presented many values of possible strains. The absence of
391 direct correlation between these two microstructural parameters could be explained by the
392 fact that a same phase fraction corresponded to many arrangements and sizes of clasts
393 (Figure 9 b,e). For example a same area fraction of clays and clasts could correspond to a
394 homogeneous concentration of small clasts in the subset, or to an aggregate of few large
395 clasts surrounded by clays.

396 **4. Discussion**

397 **4.1. A comparison between strains and microstructure on a representative area**

398 A range of representative elementary areas (REA) of phase area fraction and clast size has
399 been determined on the same multi millimeter-size surface on Tournemire clay rock, by
400 different methods such as the counting box and the dispersion methods (Fauchille, 2015;
401 Cosenza et al., 2019). Microstructural and mechanical (bulk and shear moduli) REA of
402 Tournemire clay rock have been estimated at 345 to 696 μm and 687 to 1772 μm ,
403 respectively, for relative errors of 5 to 10% (Cosenza et al., 2019). Mechanical REA are
404 then two times greater than microstructural REA, but their values support the fact that the
405 comparison between strains and microstructure of this study is representative of the
406 mesoscopic scale of Tournemire clay rock. Other studies demonstrated that for Mont-Terri
407 and Posidonia clay rocks, surfaces larger than 140 x 140 to 250 x 250 μm^2 (depending on
408 the facies) are representative of mineral area fractions in high resolution (Klaver et al. 2012,
409 Houben et al., 2014). At a similar scale and resolution, representative elementary surfaces
410 of Bowland Shale were quantified in the range of a few millimeters depending on the

411 relative error of the phase fraction determined (Fauchille et al., 2018). The quantitative
412 superimposition of strains and microstructure was only possible on a multi millimeter
413 surface, due the well-known heterogeneous texture of such rock. The surface filmed in this
414 study was significantly larger than the microstructural and mechanical REAs. The most
415 representative surface of microstructure as possible of the two microstructural parameters
416 was taken into account.

417 **4.2. Complex micro-mechanisms of deformation at the microstructure scale**

418 The results revealed the complexity of micro-mechanisms of clay rock deformation during
419 a hydric loading, at the microstructure scale. Hydric strains were very heterogeneously
420 distributed, as previous works also demonstrated (Yang et al., 2012; Wang et al., 2013,
421 2014). The local clay and clast area fractions did not control the local strains determined by
422 DIC at the scale investigated, neither the clast size, contrary to other studies on Callovo-
423 Oxfordian argillaceous rock in which hydric strains intensity and location were
424 qualitatively linked to the local mineralogy (Yang et al., 2012; Wang, 2012; Wang et al.,
425 2013). If speckle changes unlinked to deformation are removed, strains concentrated in the
426 clay matrix and at interfaces between clasts and clays. However the entire matrix showed a
427 heterogeneous behavior with often no local deformation, which suggests other control
428 factors than local clay, quartz or carbonate area fractions and, larger and/or lower scale-
429 dependent factors. This interpretation could be supported by the fact REA of microstructure
430 and REA of bulk and shear moduli are different (Cosenza et al., 2019). Moreover the
431 surface investigated here contains multi modal heterogeneities which may control very
432 different responses of the material and avoids any simple quantitative relationship between
433 strains and microstructure. The results previously shown and the existing literature
434 therefore highlighted that there was no simple link between the local strains and the
435 microstructure. Rather than looking for local factors which control the local strain values,

436 the identification of non-local microstructural factors could be an interesting aspect to focus
437 on, by using for example multi scale imaging techniques with variable resolutions.

438 Among all types of clasts, only isolated quartz tilted and detached from the surface.
439 Excluding possible polishing artefacts, clasts had then various responses due to their shape,
440 tortuosity and contacts which facilitated or not their ability to slip and move along clay
441 particles which are deforming. As Bauer-Plaindoux et al., (1998) interpreted on clay rocks
442 subjected to hydro mechanical tests and as Tran (2014) observed on natural and removed
443 clay soils; carbonates can form strong bridges against deformation as well.

444 At the clay particle scale, Ferrage et al., (2005) demonstrated that the hydration
445 mechanisms of swelling clay particles (montmorillonite) were heterogeneous during
446 hydration partly due to the nature of cation available. In addition, Menaceur et al., (2016)
447 demonstrated that drying clay rock caused a reduction of pore diameter which corresponds
448 to a decreasing thickness of clay platelets. At a larger scale, desiccation-induced shrinkages
449 parallel and perpendicular to beddings were related to different connectivities of pore
450 volumes filled by water (Ghorbani et al., 2009). The removal of water is enhanced in the
451 direction parallel to bedding, due to a higher pore connectivity. In this study, heterogeneous
452 hydric strains parallel to the bedding revealed that those strains might be also driven by a
453 heterogeneous repartition of water and pore connectivity (heterogeneous connectivity of
454 pore throat surface). Heterogeneous water transfers within the microstructure are strongly
455 suspected.

456 The desiccation process caused a deterioration of the material with clay matrix aggregation,
457 microcracks and quartz tilt, which joined the interpretation of Gasc-Barbier and Tessier
458 (2007), and Ghorbani et al. (2009). The hydric crack network following the strain
459 concentration of the same sample, was partly controlled by the spatial distribution of a
460 range of microstructural parameters: the area fraction, the mean area, the orientation, the

461 length ratio and the number of particles (Fauchille et al., 2014). Only the combination of all
462 parameters controled the crack location but none of those was a significant control factor
463 independently from the others. The local hydric crack aperture was also partly controlled by
464 the presence of interfaces of clay-rich and clay-poor zones around the cracks (Fauchille et
465 al., 2016b) even if the relationships are not well understood yet. At much higher
466 temperatures and for lower resolutions, hydric strains of Tournemire clay rock were
467 concentrated in a periodic pattern influenced by the orientation of bedding planes and at the
468 interface between the matrix and a multi millimeter carbonate aggregate (Hédan et al.,
469 2012). During heating, tortuous hydric strains of Kimmeridge clay rock were also
470 heterogeneously distributed and preferentially located at interfaces between clays and non-
471 clay phases and in organic matter (Figuroa et al., 2017). The literature highlights then vast
472 types and scales of microstructural interfaces, from the interfaces between individual
473 particles to interfaces of clay-rich and clay-poor areas, until the centimeter scale. Among
474 those scales, the microstructure has different capabilities to deform on either side of those
475 interfaces. The quantification and the location of multi scale interfaces of clay rich and clay
476 poor areas could be thus an interesting aspect to investigate on the same mosaic of SEM
477 images, to improve the understanding of the variability of microstructural scale dependent
478 factors on the local strains.

479 **4.3. Limitations of DIC at the microstructure scale**

480 The scale of the study corresponds to a limitation scale for DIC. Indeed, a well-polished
481 surface allowed the accurate segmentation of minerals but smooth surfaces of clasts were
482 not good markers for the DIC speckle. Bornert et al., (2010), Wang, (2012) and Yang et al.,
483 (2012) used surface roughness as a natural speckle but this configuration only allowed a
484 qualitative comparison between strains and microstructure because clasts cannot be clear
485 enough on the images. 2D and 3D higher resolution imaging techniques such as SEM

486 equipped with a field emission gun, transmission electronic microscopes, focused ion beam
487 SEM, X-ray nano-tomography and scanning transmission electron microscopy, have been
488 used to demonstrate that going down the scales doesn't allow the separation of clay matrix
489 and heterogeneities which are smaller and smaller deep inside the material (Ma et al., 2016,
490 2017, 2018; Keller et al., 2011, 2013). Due to multi-scale heterogeneities in clay rock, the
491 quality of the DIC speckle formed by the arrangement of mineral phases will be always
492 very heterogeneous. One part of the subsets will contain a significant variance of grey
493 levels which allows their accurate tracking from one image to another (typically where
494 smaller particles are). The other part will be composed of much larger particles represented
495 by homogeneous grey levels, for those any accurate tracking will be possible. Increasing
496 the subset size rather the image resolution is not the solution to calculate the local strain
497 because the strains cannot be separated for the clay matrix than the non-clay phases. Similar
498 speckle problems than those met in this study, will therefore happen in higher resolution.
499 Consequently there is a sort of scale limit between a "continuous" media allowing a good
500 quality speckle for which the comparison between microstructure and strains is reasonable,
501 and a "discontinuous" media composed of well-defined particles for which the comparison
502 is only local and qualitative, or should be characterized by other methods than DIC.

503 **4.4. Scaling effects on hydric strains**

504 Desiccation of clay rocks induced volumetric shrinkage associated to water flows (Gasc-
505 Barbier et al., 2000; Fauchille et al., 2016a). This phenomenon does not happen for other
506 sedimentary rocks such as sandstones or limestones in which clay fraction is very limited or
507 absent. Macroscopic desiccation-driven hardening described by a mean density rise, is
508 associated to the water content of the clay matrix. Qualitative comparisons on Callovo-
509 Oxfordian clay rock revealed that a higher hardening is associated to a higher clay content
510 (Ghorbani et al., 2009). During triaxial tests, hydro-mechanical clay properties can be more

511 or less expressed due to the geometrical arrangement of clays and clasts of carbonates
512 (Bauer-Plaindoux, 1998). Based on the results and the literature, three laboratory scales are
513 suggested:

514 • At the macroscopic scale, the deformation is partly driven by the mean ability of
515 clays to expand or shrink. This ability is partly controlled by the mean texture.
516 Heterogeneous thermo hydro mechanical behaviours of clayrock are often explained by
517 heterogeneous arrangements of minerals at smaller scales, such as centimeter-scale clasts
518 embedded in carbonate cement for example, beddings, laminae and macroscopic fractures.

519 • At the mesoscopic scale, the deformation is driven by very heterogeneous features
520 such as interfaces of phase fractions and properties, in the clay matrix and at clast's
521 boundaries. These features are too different to extract a simple linear trend between one
522 single parameter such as clay area or volume fraction, and the local strain value.

523 Note here that for these two scales, the presence of preexisting fractures due to the
524 geological history of the material or formed during sample extraction and preparation, may
525 generate preferential pathways for water transfer into the matrix during saturation and
526 desaturation. These preferential pathways for water could be linked to strain heterogeneities
527 during hydroloadings.

528 • At the clay particle scale, the deformation is also driven by a range of multiple
529 factors such as the pore distribution and connectivity, the clay anisotropy and the nature of
530 cations present in interlayers. The clay particle scale can also be separated in three different
531 scales, from the scale of clay layers, clay aggregates, and mixtures of clay aggregates and
532 very thin clasts with the same size than aggregates (Cosenza et al., 2019).

533 The hydric deformation has therefore scale-dependent controlling factors.

534 With DIC, the different scales can be compared to identify the role of microscopic
535 heterogeneities on the strains at the mesoscopic scale, and the role of mesoscopic

536 heterogeneities on the macroscopic scale. However the strains calculated will be always
537 dependent on the speckle. Such a comparison has been done by Fauchille et al., (2016) for
538 three different scales and the results revealed the overestimation of volumetric strains at the
539 largest scale investigated due to the presence of desiccation fractures detectable on the
540 sample surface at two lower scales. The different scales of clay rock cited above are each
541 very different from the others and contain specific heterogeneities, which may require
542 “model” materials (such as consolidated and saturated mixtures of sand and clays) with
543 controlled phase fractions and locations of heterogeneities, to increase the probability to
544 extract quantitative relationships between strains and microstructure.

545 A synthesis of main results and points addressed in the discussion are shown in Table 1.

546 **5. Conclusion and Perspectives**

547 A new method was presented to improve the understanding of Tournemire clay rock
548 response to a hydric loading at variable relative humidities and a constant temperature, in
549 the laboratory. The method aimed to compare quantitatively hydric strains determined by
550 digital image correlation on a sample’s surface, and microstructure determined by a 2D
551 mosaic of scanning electron microscopy images, on a high resolution multi millimeter field
552 of view. It has been applied on a representative surface of the mineral area fraction and
553 mineral size. Main results revealed that clay matrix and clasts show a very heterogeneous
554 strain distribution during desiccation. The strain values were not quantitatively and linearly
555 driven by the local area fraction of mineral phases at the study scale, which slightly changes
556 the previous suggestions of quantitative links between clay phase and deformation in clay
557 rock at this scale. Non local microstructural controls and heterogeneous water removals
558 within the porous network are suspected and will be further investigated.

559

560 **Acknowledgments**

561 The authors would like to express their acknowledgment to the NEEDS-MIPOR
562 program (Nucléaire, Energie, Environnement, Déchets, Société-Milieux POREux) and to
563 the French Institute for Nuclear Safety and Radioprotection (IRSN) for supporting and
564 funding this work.

565

566 **6. References**

567 Bauer-Plaindoux, C., Tessier, D. and Ghoreychi, M., 1998. Propriétés mécaniques des
568 roches argileuses carbonatées: importance de la relation calcite-argile. *Comptes Rendus*
569 *de l'Académie des Sciences-Series IIA-Earth and Planetary Science*, 326(4), 231-237.

570 Blüming, P., Bernier, F., Lebon, P., Martin, CD., 2007. The Excavation-Damaged Zone in
571 clay formations - Time-dependent behaviour and influence on performance assessment.
572 *Phys. Chem. Earth* 32, 588-599.

573 Boisson, J.Y., Bertrand, L., Heitz, J.F., Golvan, Y., 2001. In situ and laboratory
574 investigations of fluid flow through an argillaceous formation at different scales of space
575 and time, Tournemire tunnel, southern France. *Hydrogeology Journal*, 9(1): 108-123.

576 Bonin, B., 1998. Deep Geological Disposal in Argillaceous Formations: Studies at the
577 Tournemire Test Site. *J. Contam. Hydrol.* 35, 315-330.

578 Bornert, M., Valès, F., Gharbi, D., Nguyen Minh, D., 2010. Multiscale full-field strain
579 measurements for micromechanical investigation of the hydromechanical behaviour of
580 clayey rocks. *Strain* 46(1), 33-46.

581 Bossard, P., Meier, M.P., Moeri, A., Trick, T., Major, J.C., 2002. Geological and hydraulic
582 characterisation of the excavation disturbed zone in the Opalinus Clay of the Mont Terri
583 Rock Laboratory. *Eng. Geol.* 66(1-2), 19-38.

584 Bossart, P., Jaeggi, D., Nussbaum, C., 2017. Experiments on thermo-hydro-mechanical
585 behaviour of Opalinus Clay at Mont Terri rock laboratory, Switzerland. *Journal of Rock*
586 *Mechanics and Geotechnical Engineering*, 9(3), pp.502-510.

587 Bruck, H., McNeill, S., Sutton, M., Peters, W., 1989. Digital image correlation using
588 Newton-Raphson method of partial differential correction. *Exp. Mech.* 29, 261-267.

589 Cabrera, J., Beaucaire, C., Bruno, G., De Windt, L., Genty, A., Ramambasoa, N., Rejeb, A.,
590 Savoye, S., Volant, P., 2001. *Projet Tournemire : Synthèse des Résultats des*
591 *Programmes de Recherche 1995/1999. IRSN Report.*

592 Constantin, J., Vergely, P., Cabrera, J., 2002. Tectonique et fracturation associée dans le
593 bassin des Causses (Aveyron, France): le cas du secteur de Tournemire (Aveyron,
594 France). *Bull Soc Géol Fr* 173, 229–243.

595 Cosenza, P., Fauchille, A.L., Prêt, D., Hedan, S. and Giraud, A., 2019. Statistical
596 representative elementary area of shale inferred by micromechanics. *International*
597 *Journal of Engineering Science*, 142, 53-73.

598 Delage, P., Menaceur, H., Tang, A.M., Talandier, J., 2014. Suction effects in deep Callovo-
599 Oxfordian claystone. *Géotechnique Letters*, 4(4), pp.267-271.

600 Desrues, J., Lanier, J., Stutz, P., 1985. Localization of the deformation in tests on sand
601 sample. *Eng. Fract. Mech.* 21(4), 909-921.

602 De Windt, L., Cabrera, J., Boisson, J.Y., 1998. Hydrochemistry in an Indurated
603 Argillaceous Formation (Tournemire Tunnel Site, France). In: *Water-Rock Interaction*,
604 Editor Arehart and Hulsto, Balkema, Rotterdam, 145-148.

605 Fauchille, A.L., Hedan, S., Prêt, D., Valle, V., Cabrera, J., Cosenza, P., 2014. Relationships
606 between desiccation cracking behavior and microstructure of the Tournemire clay rock
607 by coupling DIC and SEM methods. *Proceedings of IS-Cambridge, Geomechanics from*
608 *Micro to Macro* 1-3 Sept. 2014, (2), 1421-1424.

609 Fauchille, A.L., 2015. Déterminismes microstructuraux et minéralogiques de la fissuration
610 hydrique dans les argilites de Tournemire : apports couples de la pétrographie
611 quantitative et de la corrélation d'images numériques, PhD thesis of Poitiers University
612 (France).

613 Fauchille, A.L., Hedan, S., Valle, V., Pret, D., Cabrera, J., Cosenza, P., 2016a. Multi-scale
614 study on the deformation and fracture evolution of clay rock sample subjected to
615 desiccation. *Applied Clay Science*, 132, 251-260.

616 Fauchille, A.L., Hedan, S., Valle, V., Pret, D., Cabrera, J., Cosenza, P., 2016b.
617 Relationships between cracking, strains and proportions of clay matrix and rigid
618 inclusions in Tournemire clay rock. *Proceedings of the 2nd Petrus-OPERA PhD and*,
619 p.42.

620 Fauchille, A.L., van den Eijnden, A.P., Ma, L., Chandler, M., Taylor, K.G., Madi, K., Lee,
621 P.D., Rutter, E., 2018. Variability in spatial distribution of mineral phases in the Lower
622 Bowland Shale, UK, from the mm-to μm -scale: Quantitative characterization and
623 modelling. *Marine and Petroleum Geology*, 92, 109-127.

624 Ferrage, E., Lanson, B., Sakharov, B.A., Drits, V.A., 2005. Investigation of smectite
625 hydration properties by modeling experimental X-ray diffraction patterns: part I.
626 Montmorillonite hydration properties. *Am. Mineral.* 90:1358–1374

627 Figueroa Pilz, F., Dowey, P.J., Fauchille, A.L., Courtois, L., Bay, B., Ma, L., Taylor, K.G.,
628 Mecklenburgh, J., Lee, P.D., 2017. Synchrotron tomographic quantification of strain and
629 fracture during simulated thermal maturation of an organic-rich shale, UK Kimmeridge
630 Clay. *Journal of Geophysical Research: Solid Earth*, 122(4), 2553-2564.

631 Gasc-Barbier, M., Cosenza, P., Ghoreychi, M., Chanchole, S., Tessier, D., 2000.
632 Conception d'un essai triaxial à succion contrôlée. *CR Acad Sci Earth Planet*
633 *Sci.*330:97–103.

634 Gasc-Barbier, M., Tessier D., 2007. Structural modifications of a hard deep clayey rock due
635 to hygro-mechanical solicitations. *Int J Geomech*;7(3):227–35.

636 Ghorbani, A., Zamora, M., Cosenza, P., 2009. Effects of desiccation on the elastic wave
637 velocities of clay-rocks. *International Journal of Rock Mechanics and Mining Sciences*,
638 46(8), 1267-1272

639 Hedan, S., Cosenza, P., Valle, V., Fauchille, A.L., Dudoignon, P., Cabrera, J., 2012.
640 Investigation of the damage induced by desiccation and heating of Tournemire argillite
641 using digital image correlation. *Int. J. Rock Mech. Min. Sci.* 51, 64-75.

642 Hedan, S., Fauchille, A. L., Valle, V., Cabrera, J., Cosenza, P. 2014. One-year monitoring
643 of desiccation cracks in Tournemire argillite using digital image correlation. *Int. J. Rock*
644 *Mech. Min. Sci.*, 68, 22-35.

645 Hedan, S., Valle, V., Cabrera, J., Cosenza, P., 2018. A new approach to quantify the
646 anisotropy of hydromechanical strains in clay-rock at the gallery scale. *International*
647 *Journal of Rock Mechanics and Mining Sciences*, 111, 45-53.

648 Houben, M.E., Desbois, G., Urai, J.L, 2014. A comparative study of representative 2D
649 microstructures in Shaly and Sandy facies of Opalinus Clay (Mont Terri, Switzerland)
650 inferred from BIB-SEM and MIP methods, *Marine and Petroleum Geology*, 49, 143-
651 161.

652 Keller, L.M., Holzer, L., Wepf, R., Gasser, P., Münch, B., Marschall, P., 2011. On the
653 application of focused ion beam nanotomography in characterizing the 3D pore space
654 geometry of Opalinus clay. *Physics and Chemistry of the Earth, Parts A/B/C*, 36(17-18),
655 1539-1544.

656 Keller, L.M., Schuetz, P., Erni, R., Rossell, M.D., Lucas, F., Gasser, P., Holzer, L., 2013.
657 Characterization of multi-scale microstructural features in Opalinus Clay. *Microporous*
658 *and Mesoporous Materials*, 170, 83-94.

659 Klaver, J., Desbois, G., Urai, J.L., Littke, R., 2012. BIB-SEM study of the pore space
660 morphology in early mature Posidonia Shale from the Hils area, Germany. *International*
661 *Journal of Coal Geology*, 103, 12-25.

662 Ma, L., Taylor, K.G., Lee, P.D., Dobson, K.J., Dowey, P.J., Courtois, L., 2016. Novel 3D
663 centimetre-to nano-scale quantification of an organic-rich mudstone: The Carboniferous
664 Bowland Shale, Northern England. *Marine and Petroleum Geology*, 72, 193-205.

665 Ma, L., Fauchille, A.L., Dowey, P.J., Pilz, F.F., Courtois, L., Taylor, K.G., Lee, P.D., 2017.
666 Correlative multi-scale imaging of shales: a review and future perspectives. *Geological*
667 *Society, London, Special Publications*, 454, SP454-11.

668 Ma, L., Slater, T., Dowey, P.J., Yue, S., Rutter, E.H., Taylor, K.G., Lee, P.D., 2018.
669 Hierarchical integration of porosity in shales. *Scientific reports*, 8(1), 11683.

670 Matray, J.M., Savoye, S., Cabrera, J., 2007. Desaturation and structure relationships around
671 drifts excavated in the well-compacted Tournemire's argillite (Aveyron, France). *Eng.*
672 *Geol.* 90, 1-16.

673 Menaceur, H., Delage, P., Tang, A.M., Talandier, J., 2016. The status of water in swelling
674 shales: an insight from the water retention properties of the Callovo-Oxfordian
675 claystone. *Rock Mechanics and Rock Engineering*, 49(12), 4571-4586.

676 Montes-H., H.G., Duplay, J., Martinez, L., Escoffier, S., Rousset, D., 2004. Structural
677 modifications of Callovo-Oxfordian argillite under hydration/dehydration conditions.
678 *Ap. Clay Sc.* 25, 187-194.

679 Möri, A., Bossart, P., Matray, J.M., Franck, E., Fatmi, H., Ababou, R., 2010. Mont Terri
680 Project: cyclic deformations in the Opalinus Clay. In: *proceedings of the International*
681 *Meeting of Clay in Natural and Engineered Barriers for Radioactive Waste*
682 *Confinements, Nantes 29 March-01 April 2010*, 103-124.

683 Philipp, T., Amann-Hildenbrand, A., Laurich, B., Desbois, G., Littke, R. and Urai, J.L.,
684 2017. The effect of microstructural heterogeneity on pore size distribution and
685 permeability in Opalinus Clay (Mont Terri, Switzerland): insights from an integrated
686 study of laboratory fluid flow and pore morphology from BIB-SEM images. Geological
687 Society, London, Special Publications, 454(1), 85-106.

688 Prêt, D., Sammartino, S., Beaufort, D., Meunier, A., Fialin, M., Michot, L.J., 2010. A new
689 method for quantitative petrography based on image processing of chemical element
690 maps: Part I. Mineral mapping applied to compacted bentonites. *American Mineralogist*,
691 95(10), pp.1379-1388.

692 Prêt, D., Sammartino, S., Beaufort, D., Fialin, M., Sardini, P., Cosenza, P., Meunier, A.,
693 2010. A new method for quantitative petrography based on image processing of
694 chemical element maps: Part II. Semi-quantitative porosity maps superimposed on
695 mineral maps. *American Mineralogist*, 95(10), pp.1389-1398.

696 Sutton, M.A., Wolters, W.J., Peters, W.H., Ranson, W.F., McNeill, S.R., 1983.
697 Determination of displacements using an improved digital image correlation method.
698 *Image and vision computing* 1(3), 133-139.

699 Tran, T.D., 2014. Rôle de la microstructure des sols argileux dans les processus de retrait-
700 gonflement: de l'échelle de l'éprouvette à l'échelle de la chambre environnementale
701 (Doctoral dissertation, Paris, ENMP).

702 Tsang, C.F., Bernier, F., Davies, C., 2005. Geohydromechanical processes in the
703 Excavation Damaged Zone in crystalline rock, rock salt, and indurated and plastic clays
704 - In the context of radioactive waste disposal. *Int. J. of Rock Mech. and Min. Sci.* 42(1),
705 109-125.

706 Valès, F., 2008. Modes de déformation et d'endommagement de roches argileuses
707 profondes sous sollicitations hydro-mécaniques. PhD thesis. Ecole Polytechnique,
708 Palaiseau, France.

709 Valle, V., Hedan, S., Cosenza, P., Berdjane, M., Fauchille, A-L., 2015. Digital Image
710 Correlation Development for the Study of Materials Including Multiple Crossing Cracks.
711 Experimental Mechanics 55, 379-391.

712 Wang, L., 2012. Micromechanical experimental investigation and modelling of strain and
713 damage of argillaceous rocks under combined hydric and mechanical loads, PhD thesis
714 of Ecole Polytechnique.

715 Wang, L., Bornert, M., Chanchole, S., Yang, D.S., Héripré, E., Tanguy, A., Caldemaison,
716 D., 2013. Microscale experimental investigation of the swelling anisotropy of the
717 Callovo-Oxfordian argillaceous rock. Clay Minerals 48, 391-402.

718 Wang, L., Bornert, M., Héripré, E., Yang, D.S., Chanchole, S., 2014. Irreversible
719 deformation and damage in argillaceous rocks induced by wetting and drying. Journal of
720 Applied Geophysics 107, 108-118.

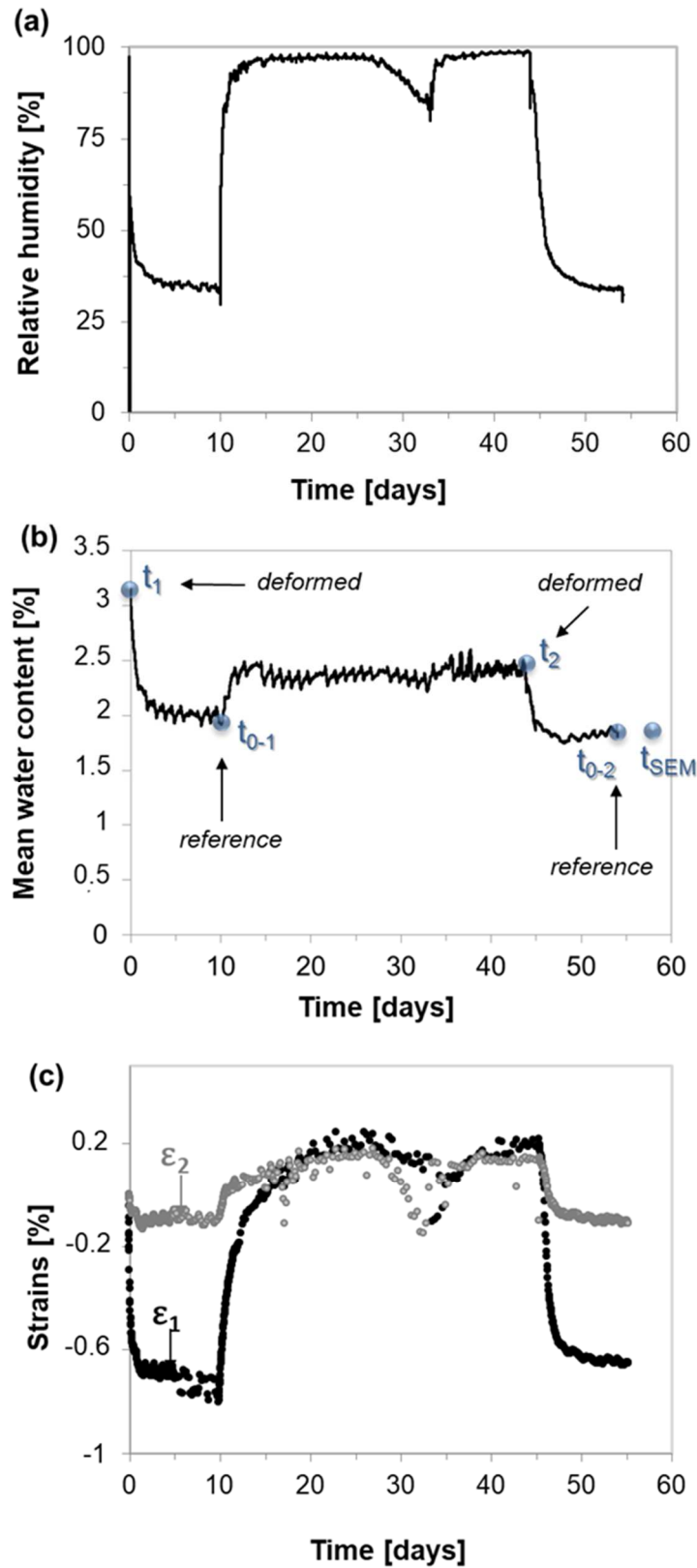
721 Yang, D.S., Bornert, M., Chanchole, S., Gharbi, H., Valli, P., Gatmiri, B., 2012.
722 Dependence of elastic properties of argillaceous rocks on moisture content investigated
723 with optical full-field strain measurement techniques. International Journal of Rock
724 Mechanics and Mining Sciences, 53, 45-55.

725

726 **List of Figures**

727 Figure 1: (a) Hydro-loading of relative humidity; (b) Mean water content of the sample as a
728 function of time and (c) Main strains as a function of time, during the whole hydric loading.
729 32
730 Figure 2: Experimental method to compare strains and microstructure quantitatively..... 33
731 Figure 3 : (a) the internal area of clasts and clays is considered to calculate **PD**, (b) the
732 entire surface of clasts is taken into account to calculate **AD**. 33

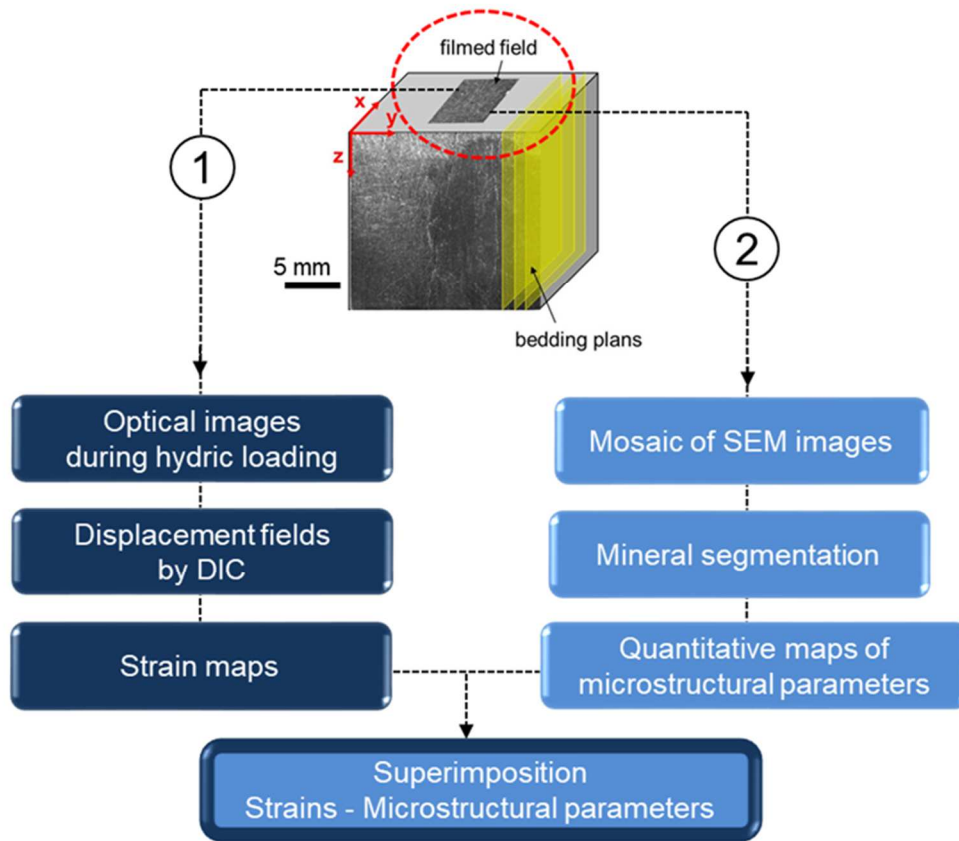
733	Figure 4: (a) Strain field of ϵ_1 , (b) high magnification view of (a), (c) strain field of ϵ_2 and	
734	(d) high magnification view of (c), for a subset of 32 pixels and the step t_{0-1} to t_1 . Ellipsoid	
735	red area 1 contains heterogeneous strains and red area 2 homogeneous strains.	34
736	Figure 5: (a) Distributions of clast area fraction values for three sizes of subset, (b) map of	
737	the clast area fraction P and (c) 2D map of clast mean area A . Subsets of 32 pixels are	
738	considered for the 2D maps.	35
739	Figure 6 : Example of superimposition of strain to microstructure between t_{0-2} and t_2 : (a)	
740	Extract of ϵ_2 strain field, (b) segmentation of minerals from the mosaic, (c)	
741	superimposition of (a) to (b).	35
742	Figure 7: (a) Variation of speckle on optical images during hydric loading, (b) Map of the	
743	standard deviation σ_{sk} of speckle between t_{0-2} and t_2 ; (c) view of (b); (d) microstructure	
744	corresponding to (b); (e) superimposition of σ_{sk} and microstructure and (f) BSE - SEM	
745	images of clasts corresponded to (e).	36
746	Figure 8: (a) Standard deviation of grey levels σ_{sk} vs the mean area of clasts between t_{0-2}	
747	and t_2 , (b) distribution of the normalized frequency of σ_{sk} for the time steps t_{0-1} to t_1 and t_{0-2}	
748	to t_2	37
749	Figure 9: (a) Main strain ϵ_1 vs area fractions of clasts and clay matrix for subsets of 32x32	
750	pixels, (b) Main strain ϵ_1 vs area fractions of clasts and clay matrix for subsets of 64x64	
751	pixels, (c) Main strain ϵ_1 vs area fraction of quartz for subsets of 32x32 pixels, (d) Main	
752	strain ϵ_1 vs area fraction of carbonates for subsets of 32x32 pixels, (e) Main strain ϵ_1 vs	
753	mean area of clasts calculated with subsets of 64x64 pixels.	38
754		



755

756 **Figure 1: (a) Hydro-loading of relative humidity; (b) Mean water content of the sample as a function of**
 757 **time and (c) Main strains as a function of time, during the whole hydic loading.**

758



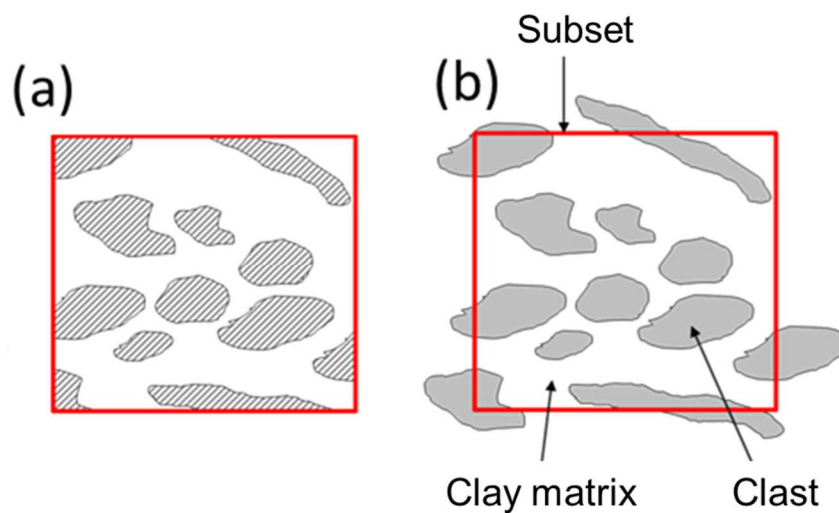
759

760

Figure 2: Experimental method to compare strains and microstructure quantitatively.

761

762



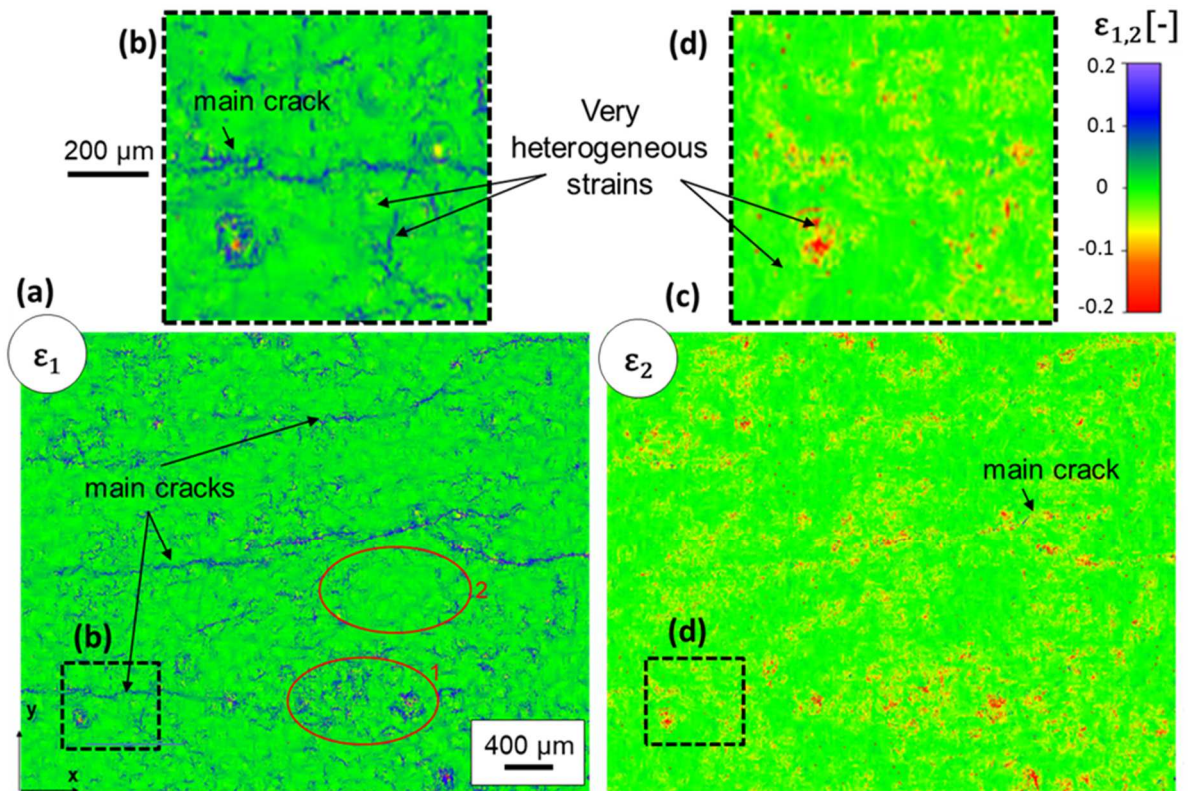
763

764

Figure 3 : (a) the internal area of clasts and clays is considered to calculate P_D , (b) the entire surface of

765

clasts is taken into account to calculate \bar{A}_D .



766

767

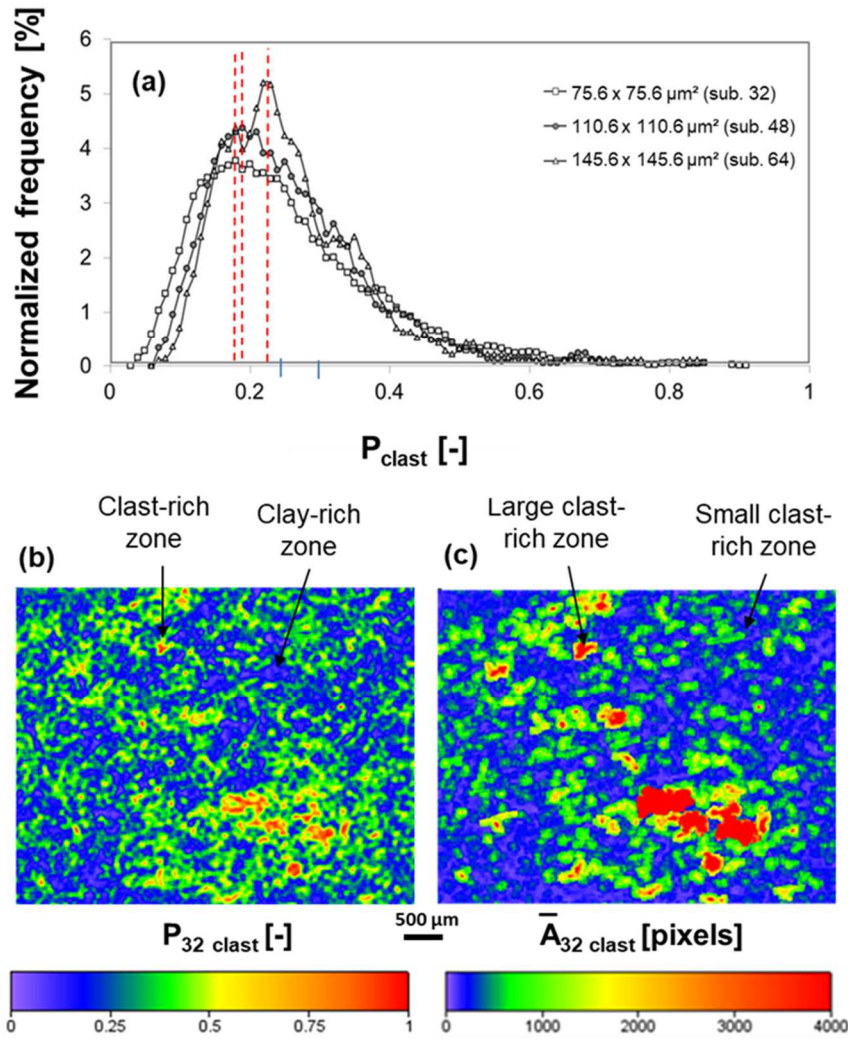
Figure 4: (a) Strain field of ϵ_1 , (b) high magnification view of (a), (c) strain field of ϵ_2 and (d) high

768

magnification view of (c), for a subset of 32 pixels and the step t_{0-1} to t_1 . Ellipsoid red area 1 contains

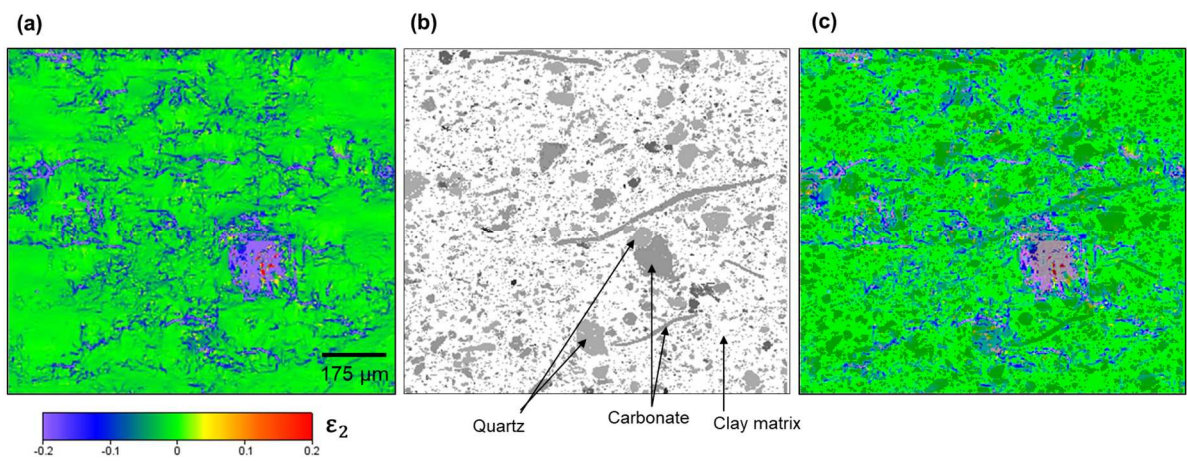
769

heterogeneous strains and red area 2 homogeneous strains.



770

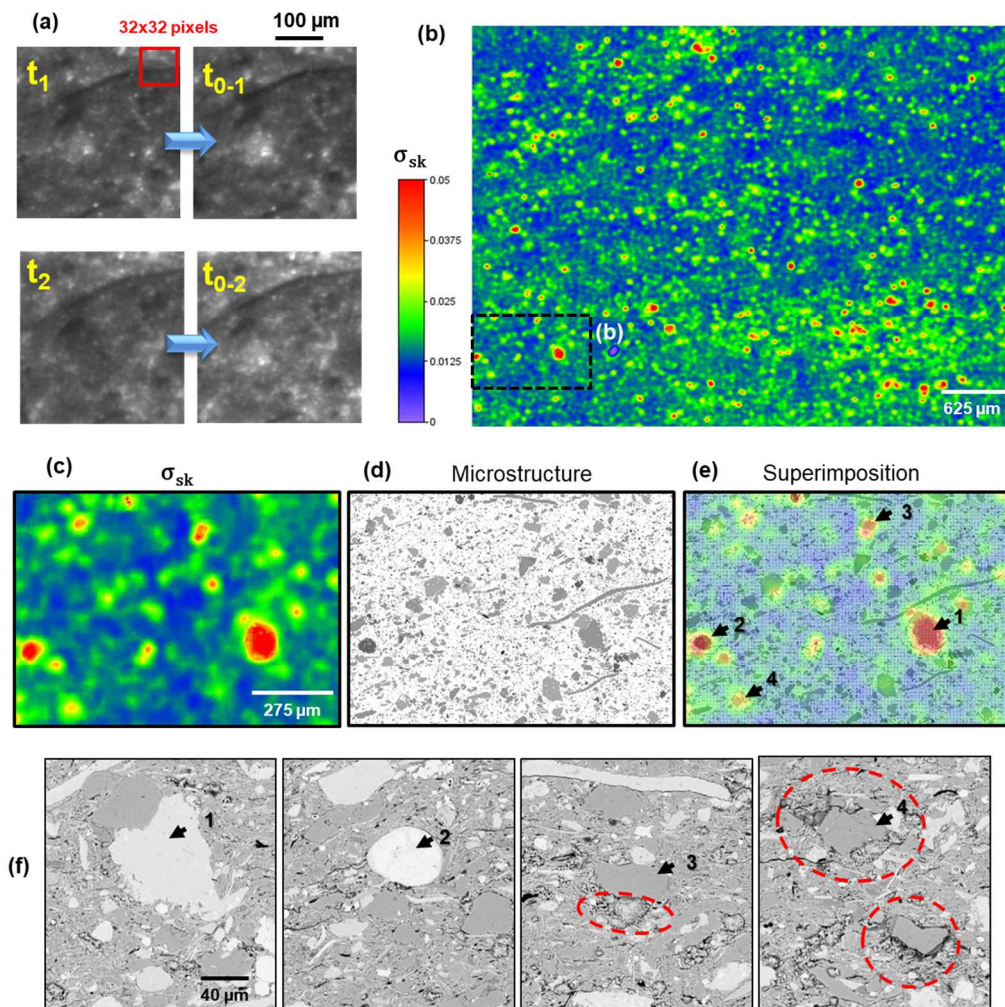
771 **Figure 5: (a) Distributions of clast area fraction values for three sizes of subset, (b) map of the clast area**
 772 **fraction P and (c) 2D map of clast mean area \bar{A} . Subsets of 32 pixels are considered for the 2D maps.**



773

774 **Figure 6 : Example of superimposition of strain to microstructure between t_{0-2} and t_2 : (a) Extract of ϵ_2**
 775 **strain field, (b) segmentation of minerals from the mosaic, (c) superimposition of (a) to (b).**

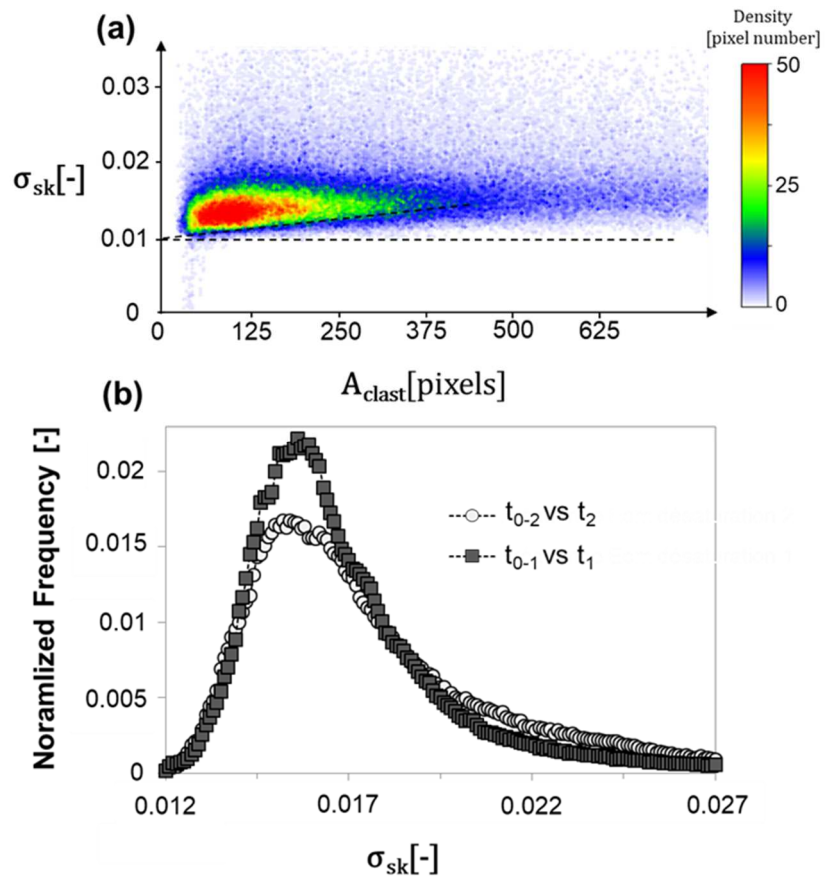
776



777

778 **Figure 7: (a) Variation of speckle on optical images during hydric loading, (b) Map of the standard**
779 **deviation σ_{sk} of speckle between t_{0-2} and t_2 ; (c) view of (b); (d) microstructure corresponding to (b); (e)**
780 **superimposition of σ_{sk} and microstructure and (f) BSE - SEM images of clasts corresponded to (e).**

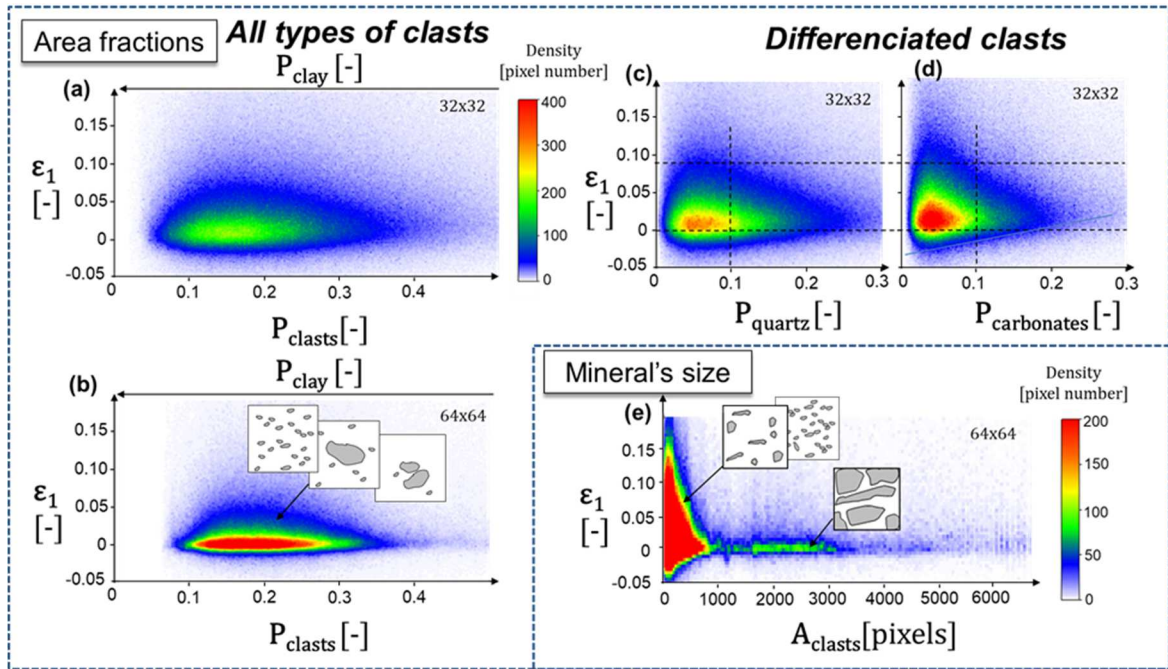
781



782

783 **Figure 8: (a) Standard deviation of grey levels σ_{sk} vs the mean area of clasts between t_{0-2} and t_2 , (b)**

784 **distribution of the normalized frequency of σ_{sk} for the time steps t_{0-1} to t_1 and t_{0-2} to t_2 .**



785

786 **Figure 9: (a) Main strain ϵ_1 vs area fractions of clasts and clay matrix for subsets of 32x32 pixels, (b)**
 787 **Main strain ϵ_1 vs area fractions of clasts and clay matrix for subsets of 64x64 pixels, (c) Main strain ϵ_1**
 788 **vs area fraction of quartz for subsets of 32x32 pixels, (d) Main strain ϵ_1 vs area fraction of carbonates**
 789 **for subsets of 32x32 pixels, (e) Main strain ϵ_1 vs mean area of clasts calculated with subsets of 64x64**
 790 **pixels.**

791

Representativeness of the comparison between strains and microstructure

Microstructural REA : REA1 = 345-696 μm^*
 Mechanical REA : REA2 = 687-1772 μm^*
 Surface investigated S = 4,1 x 5 mm^2

$$S \gg \text{REA2} > \text{REA1}$$

Complex hydromechanisms of clay rock deformation during deformation

Main results	Possible interpretations	Recommendations
(1) No linear correlation between strains and clay/clast area fraction.	Strains could be controlled by a combination of microstructural factors.	DIC might not be the best tool to determine strains at the mesoscopic scale when the surface is well-polished.
(2) No linear correlation between strains and clast size.	Heterogeneous porosity and water repartition could control local strains.	Use model clay materials with controlled microstructure to compare quantitatively local strains and microstructural parameters.
(3) Strains of clast-rich regions are wrong due to a low local contrast and an evolving speckle.		

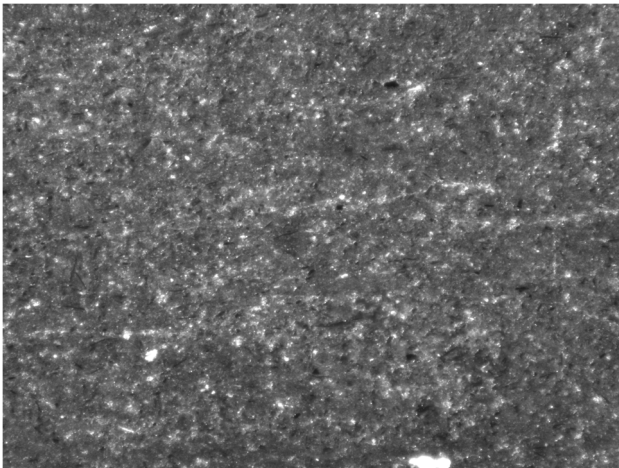
792

793

Table 1: Synthesis of results and discussion (*Cosenza et al., 2019).

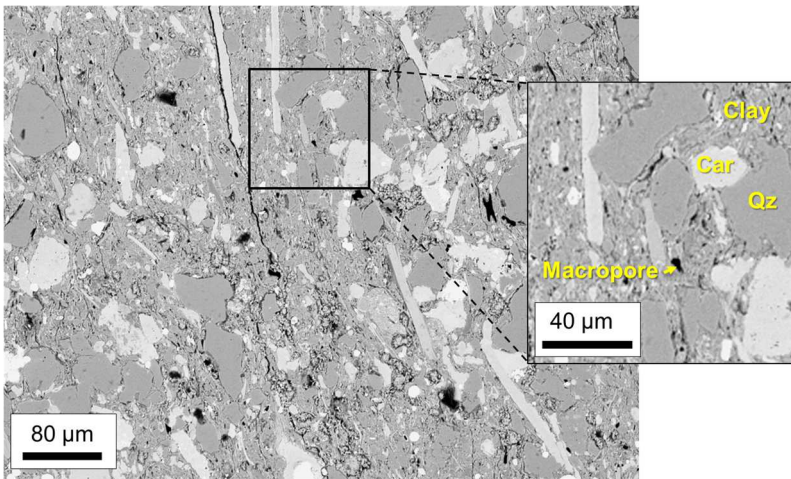
794

795 **Supplementary Material**



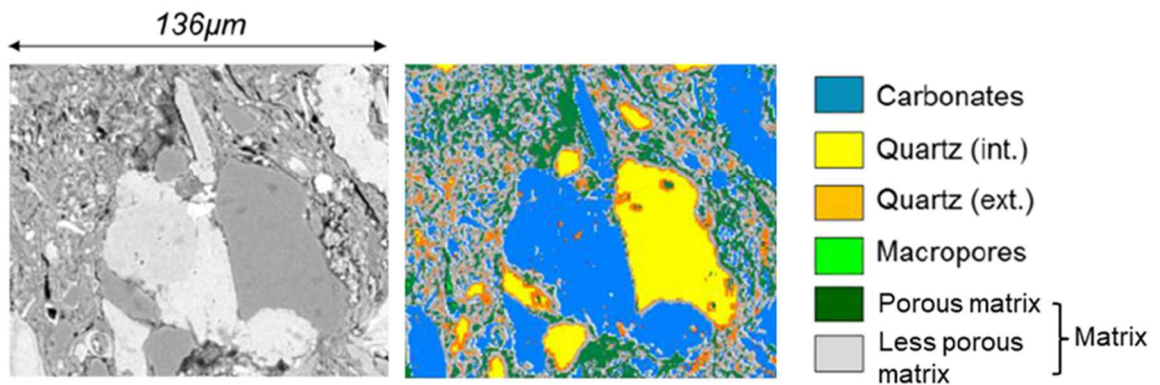
796

797 **Appendix 1: Optical image of the sample surface, at t_{0-1} .**



798

799 **Appendix 2: Microstructure of the sample after the hydric loading, BSE image extracted from the**
800 **mosaic. Clay: clay matrix, Car: carbonates, Qz : quartz.**



801

802 **Appendix 3: Phase segmentation of the SEM back scattered electron images.**